




Alloy Stability of $\text{Ge}_{1-x}\text{Sn}_x$ with Sn Concentrations up to 17% Utilizing Low-Temperature Molecular Beam Epitaxy

DANIEL SCHWARZ ^{1,2}, HANNES S. FUNK,¹ MICHAEL OEHME,¹
and JÖRG SCHULZE¹

1.—Institute of Semiconductor Engineering, University of Stuttgart, Pfaffenwaldring 47, 70569 Stuttgart, Germany. 2.—e-mail: schwarz@iht.uni-stuttgart.de

The binary alloy germanium tin has already been presented as a direct group IV semiconductor at high tin concentrations and specific strain. Therefore, it offers a promising approach for the monolithic integrated light source towards the optical on-chip communication on silicon. However, the main challenge faced by many researchers is the achievement of high tin concentrations and good crystal quality. The key issues are the lattice mismatch to silicon and germanium, as well as the limited solid solubility of tin in germanium of less than 1%. Therefore, this paper presents a systematic investigation of the epitaxial growth conditions of germanium tin with tin concentrations up to 17%. For this, we performed two growth experiments utilizing molecular beam epitaxy. In one experiment, we varied the growth temperature for the epitaxy of germanium tin with 8% tin to investigate the inter-growth temperature stability. In the second experiment, we focused on the strain-relaxation of germanium tin, depending on different tin concentrations and doping types. The results of subsequent material analysis with x-ray diffraction and scanning electron microscopy allow us to narrow the epitaxial window of germanium tin. Furthermore, we present a possible explanation for the unique relaxation mechanism of germanium tin, which is significantly different from the well-known relaxation mechanism of silicon germanium.

Key words: Silicon, germanium tin, molecular beam epitaxy, X-ray diffraction, alloy stability

INTRODUCTION

Silicon (Si), as a dominant player in semiconductor technology, suffers from an inability to achieve efficient light emission due to its indirect bandgap. Therefore, the recent increased interest in the monolithic integration of optoelectronics^{1–5} has been the driving force for research on the realization of group IV direct semiconductor behaviour on Si. Ever since the experimental demonstration of the optically pumped germanium tin ($\text{Ge}_{1-x}\text{Sn}_x$) laser,⁶ this material system has been studied as a direct

semiconductor at high Sn concentrations and specific strain.⁷

However, most research groups face the challenging epitaxy of high qualitative and relaxed Sn-rich $\text{Ge}_{1-x}\text{Sn}_x$. One of the main obstacles is the lattice mismatch of $\text{Ge}_{1-x}\text{Sn}_x$ to Si and Ge which leads to undesirable strain and later relaxation by the formation of threading dislocations and defects. Of particular concern is also the limited Sn solubility in Ge and Si of less than 1%.^{8,9} Low Sn solubility causes Sn segregation^{10,11} and in the worst case the decomposition of the alloy itself.¹² The problem is intensified due to the low melting point of Sn of $T_{\text{Sn}} = 231.9^\circ\text{C}$, compared with Si and Ge.¹³

In this paper, we present a systematic investigation of the epitaxial growth conditions of $\text{Ge}_{1-x}\text{Sn}_x$

(Received December 17, 2019; accepted April 29, 2020; published online May 14, 2020)

grown by the usage of molecular beam epitaxy (MBE). Based on two growth experiments, we discuss the effects of growth temperature, doping and strain on the inter-growth temperature stability of $\text{Ge}_{1-x}\text{Sn}_x$ alloys with Sn concentrations up to $c_{\text{Sn}} = 17\%$. Our findings allow us to narrow the epitaxial growth window of these Sn rich alloys. In this context, we also identified two key issues of current low-temperature MBE. It is still not known whether the evaporation cell radiation has an influence on the actual surface temperature at this low-temperature regime. Therefore, the second problem is the uncertainty of the actual surface temperature during growth, which complicates the observation of dynamic processes on the sample surface during the epitaxy of $\text{Ge}_{1-x}\text{Sn}_x$. This paper also addresses this question to improve the low-temperature MBE of $\text{Ge}_{1-x}\text{Sn}_x$ alloys.

EXPERIMENTAL SETUP

All discussed experiments were performed on a 6'' solid-source MBE system with a base pressure of $p_{\text{B}} = 1 \times 10^{-10}$ mbar, where Si, Ge and Sn act as matrix materials, and boron (B) and antimony (Sb) as *p*-type and *n*-type dopants, respectively. While Si was evaporated using an electron beam evaporator, Ge, Sn, B and Sb were evaporated using Knudsen effusion cells. Sample heating was performed through radiative heating using a graphite heater. Since the substrate temperature T_{Sub} is the most critical growth parameter for the epitaxy of $\text{Ge}_{1-x}\text{Sn}_x$, we used three different systems for precise substrate temperature measurement and control. For substrate temperatures $T_{\text{Sub}} > 300^\circ\text{C}$, we used a carefully calibrated thermocouple. However, substrate temperatures $T_{\text{Sub}} < 300^\circ\text{C}$ were measured with a Fluke TiS65 infrared camera (IR) with spectral responsivity of $8 \mu\text{m} \leq \lambda_{\text{res}} \leq 13 \mu\text{m}$. The emission factor was set to $\varepsilon = 0.7$, which was calibrated at higher temperatures where the thermocouple signal is still valid. For the transmission factor τ of the vacuum chamber window, we used $\tau = 0.7$.

In order to gain detailed information about the layer quality and its strain, the samples were characterized by high-resolution x-ray diffraction (HR-XRD) to perform $2\theta - \omega$ scans of the (004) reflection as well as reciprocal space maps (RSM) of the $(\bar{2}\bar{2}4)$ reflection. The HR-XRD measurements were performed on a Rigaku SmartLab diffractometer.

Furthermore, the sample surface was analysed with scanning electron microscopy (SEM). All SEM micrographs were taken using a Zeiss Gemini SEM, equipped with a Centaurus backscattered-electron (BSE) detector, which was used for topography and compositional analysis. All micrographs were acquired at an acceleration voltage $U_{\text{Acc}} = 10$ kV.

SAMPLE STRUCTURE

Buffer Layer Stack

All samples were grown on B-doped 4'' Si (001) substrates with a specific resistance of $10 \Omega \text{ cm} \leq \rho \leq 20 \Omega \text{ cm}$. The sample layer stack for the $\text{Ge}_{1-x}\text{Sn}_x$ samples is shown in Fig. 1. The epitaxy process was started with a thermal desorption step at $T_{\text{Sub}} = 900^\circ\text{C}$ to remove the native silicon dioxide (SiO_2) of the substrate surface.¹⁴ The layer stack growth was then started with a 50 nm thick Si buffer layer, grown at a substrate temperature $T_{\text{Sub}} = 600^\circ\text{C}$. In order to overcome the lattice mismatch between Si and Ge, a 100 nm-thick Ge virtual substrate (Ge-VS) was grown and subsequently annealed at a substrate temperature $T_{\text{Sub}} = T_{\text{A}} = 850^\circ\text{C}$ for $t = 5$ min to reduce the threading dislocation density.² The growth then continued with a second 400 nm-thick Ge layer, grown at a substrate temperature $T_{\text{Sub}} = 330^\circ\text{C}$, for a further reduction of the threading dislocation density and therefore improvement in the crystal quality.

$\text{Ge}_{1-x}\text{Sn}_x$ Layer Growth

In order to investigate the epitaxial breakdown and the effect of strain relaxation of $\text{Ge}_{1-x}\text{Sn}_x$, a series of 14 different $\text{Ge}_{1-x}\text{Sn}_x$ layers were grown as individual samples with a thickness of $d_{\text{GeSn}} = 200$ nm, each directly on top of the described buffer layer stack.

In the first part of the experiment, two samples with a nominal Sn concentration of $c_{\text{Sn}} = 8\%$ but with different substrate temperature profiles were grown to investigate the inter-growth temperature stability of $\text{Ge}_{1-x}\text{Sn}_x$ (see Table I). For sample 1, the

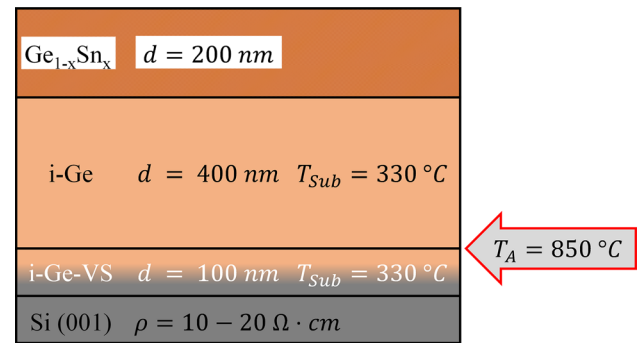


Fig. 1. Schematic layer stack of the discussed samples.

Table I. Experiment 1 $\text{Ge}_{1-x}\text{Sn}_x$ samples

Sample	c_{Sn} (%)	P_{Heater}
1	8	84 W \rightarrow 0 W
2	8	0 W

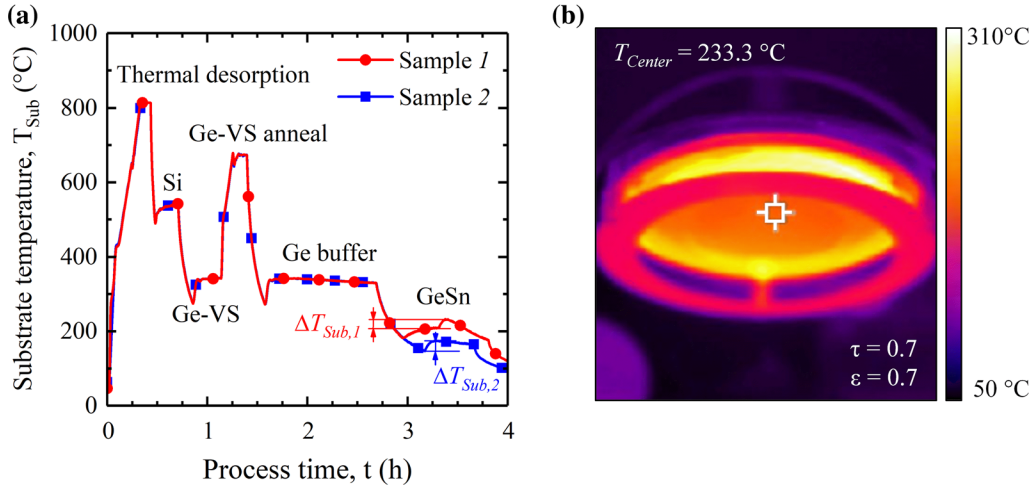


Fig. 2. (a) Comparison of the substrate temperature profile of sample 1 and sample 2. (b) Capture of the IR camera of sample 2 while the substrate temperature exceeded the melting point of Sn. $T_{\text{Sn}} = 231.9^\circ\text{C}$ during the growth of $\text{Ge}_{1-x}\text{Sn}_x$.

substrate was heated through a power ramp-down of the graphite heater from $P_{\text{Heater}} = 84\text{ W}$ to $P_{\text{heater}} = 0\text{ W}$ during the growth of the $\text{Ge}_{1-x}\text{Sn}_x$ (see Table I). In contrast to sample 1, the $\text{Ge}_{1-x}\text{Sn}_x$ of sample 2 was grown with the heater power set to zero. The observed increase in the substrate temperature of sample 2, which can be seen in Fig. 2a, was provided by the radiation of the Ge and Sn effusion cells. Throughout the process, the substrate temperature was monitored with the IR camera. For both samples, a B doping concentration of $N_{\text{A}} = 1 \times 10^{20}\text{ cm}^{-3}$ was used for the $\text{Ge}_{1-x}\text{Sn}_x$ layer.

The second part of the experiment focuses on the effect of relaxation and decomposition due to increasing strain for higher Sn concentrations c_{Sn} . For this purpose, the sample series continues with an increasing nominal Sn concentration from $8\% \leq c_{\text{Sn}} \leq 14\%$. Furthermore, the effect of *p*-type and *n*-type doping, with a doping concentration of $N_{\text{A,D}} = 1 \times 10^{20}\text{ cm}^{-3}$, was investigated in this series. A complete overview of all $\text{Ge}_{1-x}\text{Sn}_x$ samples can be seen in Table II. The samples are labelled from A-*x* to D-*x* with A–D indicating a different Sn concentration each, and *x* indicating one of the three doping types (*p*, *n* and intrinsic).

In order to exclude the temperature effect, the heating power during the $\text{Ge}_{1-x}\text{Sn}_x$ growth was always set to zero during this part of the experiment.

RESULTS

Temperature-Dependent Growth Kinetics

Figure 2a shows the comparison of the substrate temperature profile for sample 1 and sample 2, measured with the IR camera. As can be seen, the effect of the different applied heating power is significant. For sample 1, the substrate temperature during the $\text{Ge}_{1-x}\text{Sn}_x$ growth increased by

Table II. Experiment 2 $\text{Ge}_{1-x}\text{Sn}_x$ samples

Sample	c_{Sn} (%)	Doping
A-		
<i>p</i>	8	<i>p</i> -type
<i>n</i>		<i>n</i> -type
<i>i</i>		Intrinsic
B-		
<i>p</i>	10	<i>p</i> -type
<i>n</i>		<i>n</i> -type
<i>i</i>		Intrinsic
C-		
<i>p</i>	12	<i>p</i> -type
<i>n</i>		<i>n</i> -type
<i>i</i>		Intrinsic
D-		
<i>p</i>	14	<i>p</i> -type
<i>n</i>		<i>n</i> -type
<i>i</i>		Intrinsic

$\Delta T_{\text{Sub},1} = 24\text{ K}$ and exceeded the melting point of Sn $T_{\text{Sn}} = 231.9^\circ\text{C}$ before it decreased slowly to $T_{\text{Sub},1} \approx 177^\circ\text{C}$. Consequently, the growth of sample 1 can be divided into three substrate temperature regimes: The beginning, where the substrate temperature was at $T_{\text{Sub},1} \approx 209^\circ\text{C}$, already too high but still below the melting point of Sn, which led to high segregation and therefore reduced incorporation of Sn. As soon as the substrate temperature exceeded the melting point of Sn, the surface mobility of the Sn atoms was high enough to form clusters of Sn, so-called Sn droplets. In the third regime, the substrate temperature decreased and therefore the Sn incorporation increased again. An exemplary image of the IR camera, while exceeding the Sn melting point, is shown in Fig. 2b.

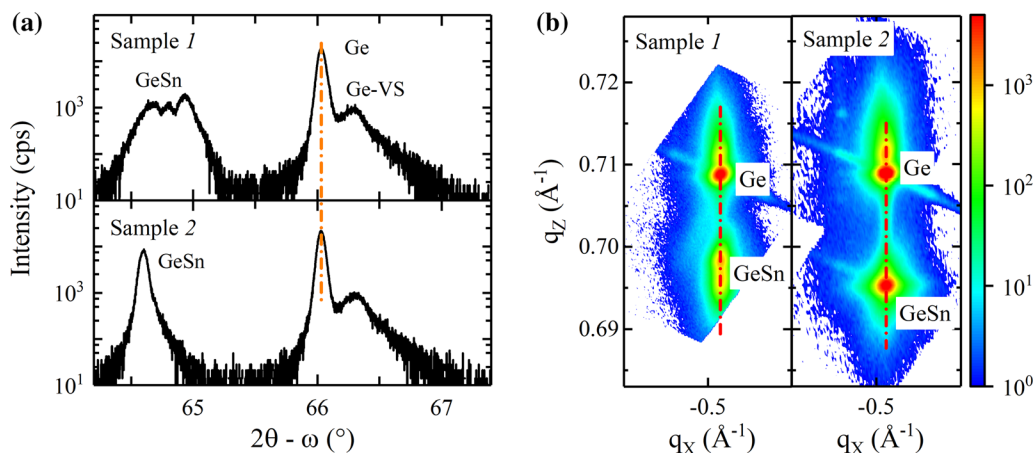


Fig. 3. (a) Comparison of the HR-XRD $2\theta - \omega$ scans of the symmetric, (004) reflection of sample 1 and sample 2. The GeSn-related reflection of sample 1 shows a significant lower intensity and a splitting into three distinguishable peaks. (b) RSMs of the asymmetric (224) reflection. For both samples, the RSM shows for sample 1 and sample 2 two reflections on the pseudomorphic line (dash-dotted red line), which can be related to the Ge buffer layer stack and the GeSn layer (Color figure online).

In contrast to sample 1, the substrate temperature during the $\text{Ge}_{1-x}\text{Sn}_x$ growth of sample 2 was always $T_{\text{Sub}} \leq 170^\circ\text{C}$. This was achieved by a longer cooling period for the substrate prior to the $\text{Ge}_{1-x}\text{Sn}_x$ growth, and by setting the heater power to zero during the $\text{Ge}_{1-x}\text{Sn}_x$ growth itself. Interestingly, the temperature profile verifies the huge influence of the effusion cell radiation on the substrate temperature. Although, the heater power was set to zero, the substrate temperature increases by $\Delta T_{\text{Sub},2} = 30\text{ K}$ during the $\text{Ge}_{1-x}\text{Sn}_x$ growth compared with the beginning of the growth itself due to the heating of the Ge effusion cell. This is a significant difference, considering the known sensitivity of Sn segregation to temperature and therefore the epitaxy of $\text{Ge}_{1-x}\text{Sn}_x$. This shows that the measurement of the substrate temperature using an IR camera allows us to observe the dynamic processes on the sample surface during low-temperature MBE.

The consequence of the three regimes of the substrate temperature, especially the exceeding of the melting point of Sn, during the growth of the $\text{Ge}_{1-x}\text{Sn}_x$ of sample 1 can be observed in Fig. 3a. It shows the HR-XRD $2\theta - \omega$ scans around the symmetric (004) reflections of the samples 1 and 2. Both samples show a double peak with an intensity gradient on the right side which can be related to the buffer layer stack of the 100 nm-thick Ge-VS with the 400 nm-thick Ge buffer layer on top. However, for lower diffraction angles, where the peaks can be associated to the $\text{Ge}_{1-x}\text{Sn}_x$ layer, the patterns of sample 1 and sample 2 show a significant difference. For sample 2, a sharp, high intense peak, correlated to the $\text{Ge}_{1-x}\text{Sn}_x$ layer, can be observed. This indicates a high crystallinity of the $\text{Ge}_{1-x}\text{Sn}_x$ layer. Interestingly, for sample 1, where the substrate temperature can be divided into three

regimes, the intensity of the peak decreases by one order of magnitude and splits into three distinguishable peaks, which can be related to the three described regimes. This is a clear indication for the reduced and then increased incorporation of Sn. However, the comparison of the RSMs in Fig. 3b shows that both layers are still pseudomorphically grown on the buffer layer stack.

In order to gain detailed information about the observed growth mechanisms and the whereabouts of the unincorporated Sn, we performed an SEM analysis of the surface of sample 1. The result of the structural analysis of sample 1 with the BSE detector in topography contrast mode is shown in Fig. 4a.

As can be seen, the sample shows structures on the surface resembling droplets (see Fig. 4a). According to the findings of our previous experiments¹⁵ and the observed substrate temperature profile, we expected the structures to be segregated Sn which formed metallic β -Sn clusters on the surface during the epitaxial growth. In order to verify this, we used the BSE detector in material contrast mode. In material contrast mode (see Fig. 4b), heavier elements appear brighter. This enabled a qualitative determination of the composition of these structures. With Sn being the heaviest element present in the sample, pure Sn should lead to a clear contrast to the surrounding sample. Figure 4b shows the result of the analysis, with the droplets appearing much brighter in the micrograph. This verifies that they consist of Sn. The Sn droplets on the surface are evidence of the described increased Sn segregation and therefore reduced Sn incorporation due to the high substrate temperature $T_{\text{Sub},1}$. There, it forms either interstitial point defects inside the alloy or Sn clusters resembling droplets on the surface.

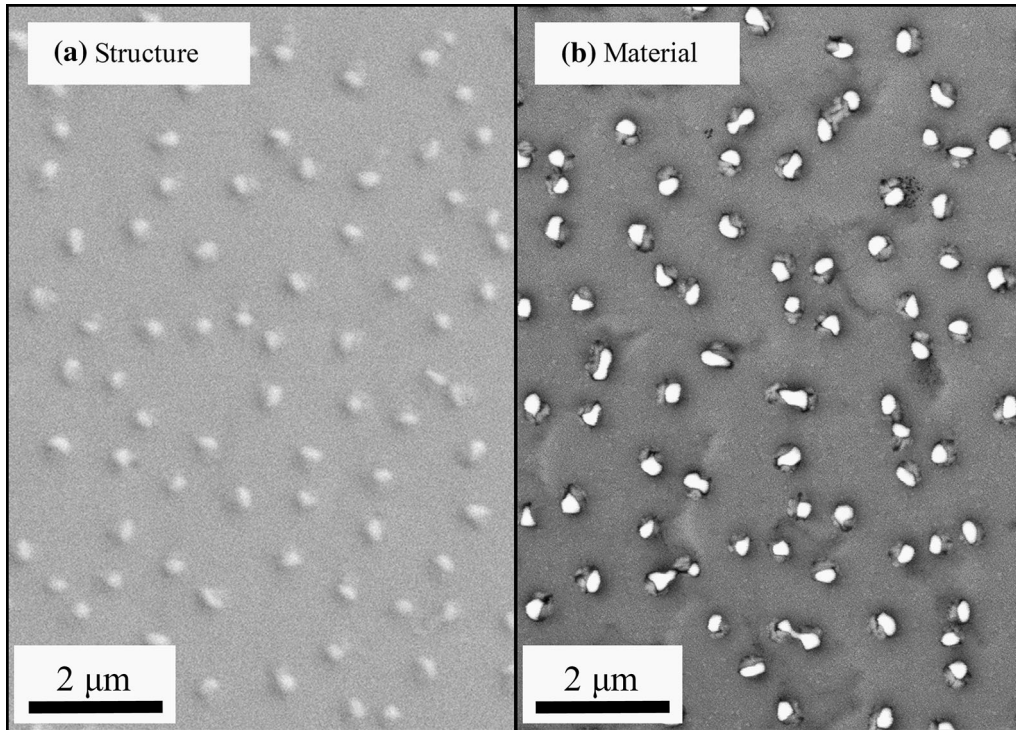


Fig. 4. SEM micrograph of sample 1 using the BSE detector in structural and material contrast mode. (a) The structural analysis of the surface shows droplet-like structures which arise from the surface. (b) The compositional analysis shows a clear contrast between the surface and the much brighter droplet structures.

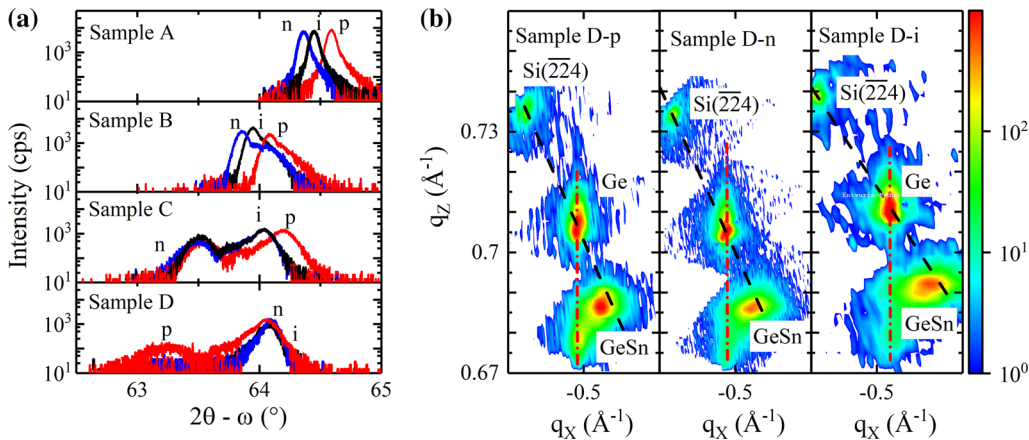


Fig. 5. (a) Comparison of the HR-XRD $2\theta-\omega$ scans of the symmetric (004) reflection of samples A, B, C and D. The $\text{Ge}_{1-x}\text{Sn}_x$ -related reflection shifts to lower angles for increasing Sn concentration. Also a different diffraction angle can be observed for the different doping types. For samples C and D with the highest Sn concentrations, the $\text{Ge}_{1-x}\text{Sn}_x$ -related reflection splits off into two reflections due to the beginning of relaxation of the $\text{Ge}_{1-x}\text{Sn}_x$ layer. (b) RSMs of the asymmetric (224) reflection shows the GeSn-related asymmetric reflection on the relaxation line (dashed black line) with a smear-out of the reflection at the pseudomorphic line (dash-dotted red line) (Color figure online).

Composition-Dependent Strain Relaxation

In the second part of the experiment, we investigated the composition-dependent effect and the mechanism behind the strain relaxation of $\text{Ge}_{1-x}\text{Sn}_x$, while the substrate temperature during the $\text{Ge}_{1-x}\text{Sn}_x$ growth was carefully kept at $T_{\text{Sub}} \leq 170^\circ\text{C}$ for this investigation. Figure 5a shows a complete overview of all HR-XRD $2\theta - \omega$ scans around the symmetric (004) reflections of the

samples A–D according to Table II. For clarity, the overview is divided into four separate graphs one for each sample. Each individual graph shows the different doping types *p*-, *n*-type and intrinsic for the same nominal Sn concentration c_{Sn} .

As expected, the peak, which can be correlated to the $\text{Ge}_{1-x}\text{Sn}_x$ layer, shifts to lower diffraction angles for higher Sn concentrations c_{Sn} . Besides that, the $\text{Ge}_{1-x}\text{Sn}_x$ associated peak shows a shift towards higher angles for *p*-type doping. Since we use B for

p-type doping, its smaller bonding length compared with Ge and Sn reduces the average lattice constant a_0 of the crystal, which causes a shift of the (004) reflection towards higher angles. The opposite effect can be observed for the *n*-type doped Ge_{1-x}Sn_x layers, where Sb was used. Sample *A* shows a very sharp and intense Ge_{1-x}Sn_x-related peak, which indicates good crystal quality. However, the peak intensity decreases while the peak shape broadens for sample *B* with increasing Sn concentration. This is clear evidence for decreasing crystal quality and the beginning of defect formation. Further increasing the Sn concentration leads to a splitting of the Ge_{1-x}Sn_x associated peak, which could be an indication of the reduced Sn incorporation due to segregation, similar to the observations of the previous experiment. Interestingly, the RSMs of the asymmetric (224) reflection of sample *D* (see Fig. 5b) present, in contrast to the expectation, the beginning strain relaxation of the layers.

Further evaluation of the RSMs allowed us to extract the in-plane lattice constant a_{\parallel} and out-of-plane lattice constant a_{\perp} of the asymmetric ($\bar{2}24$) reflection of the Ge_{1-x}Sn_x layers. The lattice parameters a_{\parallel} and a_{\perp} were then used to calculate the relaxed lattice constant a_0 of the Ge_{1-x}Sn_x layers by Eq. 1

$$a_0 = \frac{a_{\perp} + 2\mu a_{\parallel}}{1 + 2\mu} \quad (1)$$

In this equation, μ represents the composition-dependent ratio of the two elastic constants C_{12} and C_{11} . The compositional dependence of μ can be expressed by quadratic interpolation of the values for Ge and α -Sn with the Sn concentration $c_{\text{Sn}} = x$ in Eq. 2 according to Ref. 16

$$\mu = \frac{C_{12}}{C_{11}} = 0.3738 + 0.1676 \cdot x - 0.0296 \cdot x^2. \quad (2)$$

The relaxed lattice constant a_0 was then used to calculate the in-plane strain ε_{\parallel} using Eq. 3 and the actual Sn concentration $c_{\text{Sn,A}}$ using Vegard's law.

$$\varepsilon_{\parallel} = \frac{a_{\parallel} - a_0}{a_0} \quad (3)$$

Since the Sn concentration $c_{\text{Sn,A}} = x$ is needed in the first place to calculate the elastic constant ratio μ , we decided to calculate μ by an iteration method. As the initial value of $c_{\text{Sn,A}}$, we used the nominal Sn concentration c_{Sn} . It can be observed that the relative alteration of the result after three iterations is in the range of 1×10^{-6} , which proves the validity of the method.

From Table III, which shows all evaluated parameters of the Ge_{1-x}Sn_x samples, we can see that the samples *B*, *C* and *D* show a higher actual Sn concentration $c_{\text{Sn,A}}$ than the nominal value c_{Sn} , which can be explained by a deviation of the Sn effusion cell calibration. Due to the limitation of the growth temperature to $T_{\text{Sub}} \leq 170^\circ\text{C}$, samples *A*–*D* do not suffer from alloy decomposition as observed for sample *I*. Instead, the RSMs in Fig. 5b and the calculated in-plane strain ε_{\parallel} of sample *D* show almost full relaxation of the Ge_{1-x}Sn_x layer. However, the layer shows only partial relaxation. Although the Ge_{1-x}Sn_x associated peak in the RSM is located on the relaxation line, it shows a clear smear-out towards the pseudomorphic line. Considering these results for the RSMs, the presence of distinguishable peaks in the $2\theta - \omega$ scans of samples *C* and *D* can be explained by the presence of

Table III. Results for the second part of the experiment

Sample	Doping	Nominal c_{Sn} (%)	Actual $c_{\text{Sn,A}}$ (%)	In-plane strain ε_{\parallel} (%)
A-				
<i>p</i>	<i>p</i> -type	8	7.37	-1.02
<i>n</i>	<i>n</i> -type		8.74	-1.28
<i>i</i>	Intrinsic		8.49	-1.21
B-				
<i>p</i>	<i>p</i> -type	10	10.17	-1.39
<i>n</i>	<i>n</i> -type		12.46; 11.43	-0.71; -1.50
<i>i</i>	Intrinsic		11.02	-1.56
C-				
<i>p</i>	<i>p</i> -type	12	13.49; 13.24	-0.62; -1.77
<i>n</i>	<i>n</i> -type		14.08; 13.93	-0.78; -1.69
<i>i</i>	Intrinsic		14.02; 13.86	-0.92; -1.84
D-				
<i>p</i>	<i>p</i> -type	14	15.84; 15.26	-0.49; -2.14
<i>n</i>	<i>n</i> -type		16.21	-0.39
<i>i</i>	Intrinsic		16.95	-0.15

Values for actual Sn concentration $c_{\text{Sn,A}}$ and in-plane strain ε_{\parallel} for samples *A*–*D*. Multiple values, separated by semicolons, represent the values for individual identifiable peaks in the RSM

two distinguishable $\text{Ge}_{1-x}\text{Sn}_x$ layers with different strain. While a part of the $\text{Ge}_{1-x}\text{Sn}_x$ layer on top of the sample shows almost full relaxation, another part underneath seems to stay pseudomorphic. However, the clear gradient between the two peaks in the $2\theta - \omega$ scans, and furthermore the smear-out of the peak in the RSM, indicates that there is a fluent transition from full pseudomorphism to full relaxation.

This is a significant difference from the well-known relaxation mechanism of SiGe, where the layer shows full relaxation as soon as the critical thickness has been exceeded. A possible explanation for this novel relaxation mechanism is the limited thermal energy due to the low substrate temperature during the $\text{Ge}_{1-x}\text{Sn}_x$ growth process. The relaxation process starts as soon as the layer thickness d_{GeSn} exceeds the critical thickness d_{crit} of the alloy at specific Sn concentration by the formation of dislocations. However, the formation of dislocations requires a specific amount of energy which is not provided due to the low inter-growth substrate temperature.

CONCLUSION

The aim of the current study was to systematically investigate the temperature-dependent growth kinetics of $\text{Ge}_{1-x}\text{Sn}_x$ alloys on Ge-VS with Sn concentrations up to $c_{\text{Sn}} = 17\%$ by utilizing MBE. For this purpose, we performed two different experiments, where we varied the substrate temperature T_{Sub} as well as the Sn concentration c_{Sn} . Furthermore, we presented a substrate temperature measurement method using an IR camera, which allowed us to observe dynamic processes on the substrate surface during growth to improve the low-temperature MBE of $\text{Ge}_{1-x}\text{Sn}_x$ for the subsequent research experiments. The first experiment confirmed the sensitive Sn segregation, which reacts drastically to the observed dynamic changes in the substrate temperature. This leads to a reduced Sn incorporation and even the formation of Sn droplets on the growth surface when the substrate temperature exceeds the melting point of Sn.

The findings of our second experiment showed that the inter-growth alloy stability of $\text{Ge}_{1-x}\text{Sn}_x$ is independent of the Sn concentration c_{Sn} as long as the substrate temperature is kept at $T_{\text{Sub}} \leq 170^\circ\text{C}$. The results rather revealed the unique relaxation mechanism of $\text{Ge}_{1-x}\text{Sn}_x$, where only a part of the layer relaxes while a pseudomorphic part remains underneath. This is in complete contrast to the well-known relaxation mechanism of the $\text{Ge}_{1-x}\text{Sn}_x$ -related alloy SiGe.

Further experiments, using a wider parameter range, could provide a deeper understanding of the relaxation mechanism of $\text{Ge}_{1-x}\text{Sn}_x$. This is required for the growth of fully relaxed $\text{Ge}_{1-x}\text{Sn}_x$ buffer layers, which enables the fabrication of fully integrable electrically driven direct-bandgap $\text{Ge}_{1-x}\text{Sn}_x$ light emitters.

ACKNOWLEDGMENTS

Open Access funding provided by Projekt DEAL.

OPEN ACCESS

This article is licensed under a Creative Commons Attribution 4.0 International License, which permits use, sharing, adaptation, distribution and reproduction in any medium or format, as long as you give appropriate credit to the original author(s) and the source, provide a link to the Creative Commons licence, and indicate if changes were made. The images or other third party material in this article are included in the article's Creative Commons licence, unless indicated otherwise in a credit line to the material. If material is not included in the article's Creative Commons licence and your intended use is not permitted by statutory regulation or exceeds the permitted use, you will need to obtain permission directly from the copyright holder. To view a copy of this licence, visit <http://creativecommons.org/licenses/by/4.0/>.

REFERENCES

1. M. Oehme, J. Werner, M. Jutzi, G. Wöhl, E. Kasper, and M. Berroth, *Thin Solid Films* 508, 393 (2006).
2. M. Oehme, J. Werner, M. Kaschel, O. Kirfel, and E. Kasper, *Thin Solid Films* 517, 137 (2008).
3. Y.-H. Kuo, Y.K. Lee, Y. Ge, S. Ren, J.E. Roth, T.I. Kamins, D.A.B. Miller, and J.S. Harris, *IEEE J. Sel. Top. Quantum Electron.* 12, 1503 (2006).
4. M. Oehme, K. Kostecki, M. Schmid, M. Kaschel, M. Gollhofer, K. Ye, D. Widmann, R. Koerner, S. Bechler, E. Kasper, and J. Schulze, *Appl. Phys. Lett.* 104, 161115 (2014).
5. R. Koerner, D. Schwaiz, I.A. Fischer, L. Augel, S. Bechler, L. Haenel, M. Kern, M. Oehme, E. Rolseth, B. Schwartz, D. Weisshaupt, W. Zhang, and J. Schulze, in *2016 IEEE International Electron Devices Meeting (IEDM)* (2016), pp. 22.5.1–22.5.4.
6. S. Wirths, R. Geiger, N. von den Driesch, G. Mussler, T. Stoica, S. Mantl, Z. Ikonik, M. Luysberg, S. Chiussi, J.M. Hartmann, H. Sigg, J. Faist, D. Buca, and D. Grützmacher, *Nat. Photonics* 9, 88 (2015).
7. L. Jiang, J.D. Gallagher, C.L. Senaratne, T. Aoki, J. Matthews, J. Kouvetakis, and J. Menéndez, *Semicond. Sci. Technol.* 29, 115028 (2014).
8. R.W. Olesinski and G.J. Abbaschian, *Bull. Alloy Phase Diagr.* 5, 265 (1984).
9. R.W. Olesinski and G.J. Abbaschian, *Bull. Alloy Phase Diagr.* 5, 273 (1984).
10. E. Kasper, J. Werner, M. Oehme, S. Escoubas, N. Burle, and J. Schulze, *Thin Solid Films* 520, 3195 (2012).
11. H. Li, C. Chang, T.P. Chen, H.H. Cheng, Z.W. Shi, and H. Chen, *Appl. Phys. Lett.* 105, 151906 (2014).
12. M. Oehme, K. Kostecki, M. Schmid, F. Oliveira, E. Kasper, and J. Schulze, *Thin Solid Films* 557, 169 (2014).
13. B. Predel, in *Ac-Ag... Au-Zr*, edited by B. Predel (Springer, Berlin, 2006), pp. 1–23.
14. E. Kasper, M. Bauer, and M. Oehme, *Thin Solid Films* 321, 148 (1998).
15. L. Kormoš, M. Kratzer, K. Kostecki, M. Oehme, T. Šikola, E. Kasper, J. Schulze, and C. Teichert, *Surf. Interface Anal.* 49, 297 (2017).
16. R. Beeler, R. Roucka, A.V.G. Chizmeshya, J. Kouvetakis, and J. Menéndez, *Phys. Rev. B* 84, 035204 (2011). <https://doi.org/10.1103/PhysRevB.84.035204>.

Publisher's Note Springer Nature remains neutral with regard to jurisdictional claims in published maps and institutional affiliations.